Opto-Electronic Advances

Article

November 2023, Vol. 6, No. 11

DOI: 10.29026/oea.2023.230018

Spatiotemporal hemodynamic monitoring via configurable skin-like microfiber Bragg grating group

Hengtian Zhu[1†], Junxian Luo[2†], Qing Dai[3†], Shugeng Zhu[1], Huan Yang[1], Kanghu Zhou[1], Liuwei Zhan[1], Biao Xu[3], Ye Chen[1], Yanqing Lu[1] and Fei Xu[1*]

Systemic blood circulation is one of life activity's most important physiological functions. Continuous noninvasive hemodynamic monitoring is essential for the management of cardiovascular status. However, it is difficult to achieve systemic hemodynamic monitoring with the daily use of current devices due to the lack of multichannel and time-synchronized operation capability over the whole body. Here, we utilize a soft microfiber Bragg grating group to monitor spatiotemporal hemodynamics by taking advantage of the high sensitivity, electromagnetic immunity, and great temporal synchronization between multiple remote sensor nodes. A continuous systemic hemodynamic measurement technique is developed using all-mechanical physiological signals, such as ballistocardiogram signals and pulse waves, to illustrate the actual mechanical process of blood circulation. Multiple hemodynamic parameters, such as systemic pulse transit time, heart rate, blood pressure, and peripheral resistance, are monitored using skin-like microfiber Bragg grating patches conformally attached at different body locations. Relying on the soft microfiber Bragg grating group, the spatiotemporal hemodynamic monitoring technique opens up new possibilities in clinical medical diagnosis and daily health management.

Keywords: spatiotemporal hemodynamic monitor; skin-like photonic devices; microfiber Bragg grating

Zhu HT, Luo JX, Dai Q, Zhu SG, Yang H et al. Spatiotemporal hemodynamic monitoring via configurable skin-like microfiber Bragg grating group. *Opto-Electron Adv* **6**, 230018 (2023).

Introduction

Cardiovascular disease is the world's leading cause of death[1]. According to the World Health Organization, 17.9 million people die every year due to cardiovascular diseases such as coronary heart disease, cerebrovascular disease, peripheral arterial disease, thromboembolic disease, etc. For the prewarning and accurate treatment of cardiovascular diseases, it is important to monitor hemodynamic parameters continuously, including blood pressure (BP), heart rate (HR), peripheral resistance (PR), and vascular elasticity. Several available physiological signals, such as electrocardiogram (ECG) signals[2], phonocardiogram (PCG) signals[3], and pulse waves[4,5] can be used to calculate specific hemodynamic parameters

[1]College of Engineering and Applied Sciences and Collaborative Innovation Center of Advanced Microstructures, Nanjing University, Nanjing 210023, China; [2]School of Physics, Nanjing University, Nanjing 210023, China; [3]Department of Cardiology, Affiliated Drum Tower Hospital, Medical School of Nanjing University, Nanjing 210008, China.

[†]These authors contributed equally to this work.

*Correspondence: F Xu, E-mail: feixu@nju.edu.cn

Received: 7 February 2023; Accepted: 15 April 2023; Published online: 26 July 2023

and diagnose diseases such as arrhythmia and myocardial infarction. Pulse transit time (PTT), the time it takes for an arterial pulse wave to reach the periphery, can continuously and noninvasively evaluate BP without a cuff[6–11]. Soft wearable devices are well suited to monitoring physiological signals with the advantages of real-time operation capability, skin-like mechanical properties, and high-SNR sensing capability[12–22]. However, the human cardiovascular system is complicated and distributed. Monolithic hemodynamic parameters achieved by current wearable devices cannot adequately and precisely reflect the health status of regional vasculature. A spatiotemporal hemodynamic monitoring technique is urgently needed to satisfy the ever-growing demand for clinical treatment and daily health management of the cardiovascular system.

The distributed optical fiber (DOF) sensing technique represented by the fiber Bragg grating (FBG) is ideally suited for spatiotemporal hemodynamic monitoring. Its spatially distributed multichannel sensing capability and lack of electromagnetic interference lay a foundation for multiple high-SNR physiological signal monitoring[23–25]. The excellent time synchronization ensures PTT detection accuracy considering the fast pulse wave velocity (PWV). In addition, the flexible networking of FBGs can customize a sensing net on the body according to hemodynamic monitoring requirements. However, the traditional optical fiber has a large-distinct mechanical property with the skin considering its rigid and brittle silica material and thick diameter of 125 μm, making it difficult to be worn on the body stably and comfortably. Flexible packaging technology has been used to address the mechanical mismatch[26–28]. Nevertheless, excessive thick encapsulation and the low sensitivity of commercial FBG devices pose obstacles in detecting subtle physiological signals, thereby limiting their potential applications in wearable devices. Optical microfibers have been proven to have excellent flexibility, configurability, and large evanescent fields for high sensitivity sensing. In recent years, flexible devices based on microfibers have realized physiological signal monitoring[19,29], voice detection[21], and human-computer interaction[30]. However, these devices are difficult to achieve spatially distributed, time-synchronized, and multi-parameter sensing capability without wavelength encoding strategy.

Here, we report a configurable soft microfiber Bragg grating (μFBG) group to monitor spatiotemporal hemodynamics. The precise tapering technology, flexible packaging technology, and advanced femtosecond laser direct-writing technique were employed to prepare the skin-like μFBG patch. Due to the ultrafine diameter and ultrathin thickness, the patch has excellent flexibility and enhanced sensitivity by two orders of magnitude. A ballistocardiogram (BCG) signal is successfully detected by a μFBG patch attached to the chest skin at the tricuspid site. Pulse waves at different superficial artery sites are detected with a high signal-to-noise ratio. The soft μFBG group can be constructed by connecting μFBG patches in series. Benefiting from the flexible layout of the soft μFBG group on the body, systemic PTTs are calculated, revealing the health status of regional arteries. HR and BP, two important hemodynamic parameters, are monitored when the user exercises. Moreover, the variation in regional PR can be detected. Relying on the soft μFBG group, the spatiotemporal hemodynamic monitoring technique opens up new possibilities in daily health management, early screening of disease, and precise treatment in the clinic. Table S1 summarizes the differences of this work from previous studies based on the microfiber sensors.

Results and discussion

Device design and working principle

The optical microfiber contains a femtosecond laser-inscribed FBG embedded in a skin-like thin polydimethylsiloxane (PDMS) patch and is connected end-to-end with two commercial single-mode optical fibers (SMFs) for light propagation, as shown in Fig. 1(a). The optical micrograph in Fig. 1(b) and scanning electron micrograph (SEM) in Fig. 1(c) show that the microfiber has a controllable and uniform diameter of 12 μm using the flame brushing method[31] (for the detailed fabrication process, see Supplementary information Fig. S1). The smooth surface of the microfiber ensures the low loss of the μFBG patch. The optical microfiber has great flexibility and configurability due to its ultrafine diameter[29,32]. The ultrathin PDMS patch prepared by the scraper-coating flexible packaging technique provides a similar elastic modulus to human skin and a large lamination area, ensuring strong adhesion. Additionally, PDMS has a lower refractive index than the microfiber and serves as the cladding layer of the optical waveguide. This restricts the evanescent field of the microfiber and ensures low loss of the μFBG patch. As shown in Fig. 1(d), the skin-like μFBG patch is capable of attaching to a model hand

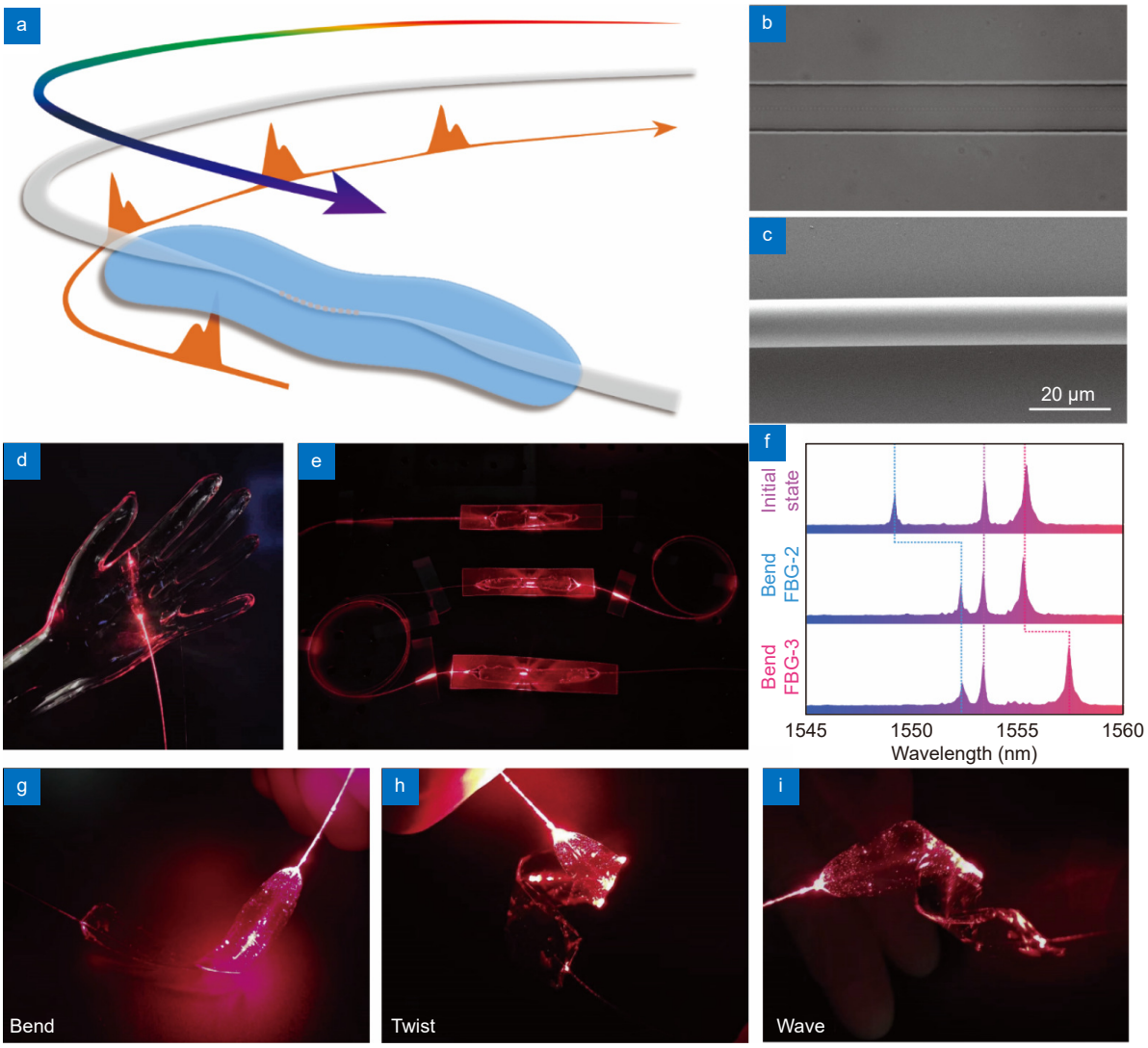

Fig. 1 | Skin-like microfiber Bragg grating (μFBG) patch. (**a**) Schematic illustration of the soft μFBG patch. The optical microfiber contains a femtosecond laser-inscribed FBG embedded in a thin PDMS patch and is connected end-to-end with two commercial single-mode optical fibers (SMFs) for light propagation. (**b**) Optical micrograph of the soft μFBG patch. The FBG is inscribed in the axis of the microfiber. (**c**) SEM of the microfiber, which has a diameter of 12 μm. (**d**) Image of the soft μFBG patch draped on a life-sized, transparent mannequin hand conformally. (**e**) Image of three soft μFBG patches connected in series to illustrate the multichannel sensing capabilities. (**f**) Reflective optical spectrum of the three soft μFBG patches. The μFBG patches are capable of detecting strain separately without interference due to the different working wavelengths. (**g–i**) Images of the soft μFBG patch under modes of bending, twisting, and waving, demonstrating the mechanical compliance and robustness of the device.

conformally. Using the femtosecond laser direct-writing technique[33,34], the FBG is inscribed at the axis of the microfiber point by point, avoiding the damage of the peripheral PDMS patch. The working wavelength of FBG can be controlled by the grating period when the microfiber's diameter is fixed. As shown in Fig. 1(e), three soft μFBG patches with different working wavelengths are connected in series by a commercial single-mode fiber, making multichannel operation over the whole body possible. A red light propagates along the optical fiber and scatters out at the three FBG positions. The reflective optical spectra of the three soft μFBG patches can be acquired with a single measurement using the optical signal acquisition such as the optical spectrum analyzer (OSA) and FBG interrogator, ensuring excellent temporal synchronization. When bending one of the soft μFBG patches, its grating period changes, resulting in the wavelength shift of the corresponding reflective peak in the optical spectrum without interference with the other reflective peaks (Fig. 1(f)). The total transmission loss of the three μFBG patches is 1.95 dB (0.65 dB each on average), indicating the low loss of the skin-like μFBG patch.

As shown in Fig. 1(g–i), regardless of bending, twisting, or waving the soft μFBG patch, it can withstand deformation and guide light, showing its high potential for skin integration applications.

Device characterization

The skin-like μFBG patch converts strain to a shift in the working wavelength, realizing force/vibration sensing. Its response to the stress and vibration was characterized by the stress test equipment (Supplementary information Fig. S2). The soft μFBG patch was attached to a thick Ecoflex (smooth-on 00-30) substrate, which had a low elastic modulus (69 kPa under 100% strain) and was used to simulate human skin. An Ecoflex contactor was employed to compress the soft μFBG patch, resulting in different degrees of deformation. Figure 2(a) shows the reflective optical spectrum under different stresses. The raw curves (light color) were fitted with the Lorentz function to extract the peak wavelengths. The reflective peak shifted right significantly when the stress increased. According to Fig. 2(b) and Fig. 2(c), the soft μFBG patch had a high and linear sensitivity of 5.26 nm/N under a small stress range (within 50 mN) and a high sensitivity of 2.86 nm/N under a large stress range (0.05–0.45 N). The sensitivity guaranteed the signal quality for human physiological signals such as a pulse wave (10–50 mN). The stress response curves when stress increased and decreased are identical in Fig. 2(d), indicating the low hysteresis property. Figure 2(e) demonstrates the dynamic response under multiple different stresses. The wavelength shift was identical to the stress calibrated by a commercial force meter and showed good repeatability and stability. Using the same characterization method, the commercial FBG with diameters of 125 μm and 80 μm had low sensitivities of 0.02 nm/N and 0.04 nm/N, respectively (Fig. 2(b), inset). The stress response of the soft μFBG patch was enhanced by 2 orders of magnitude compared with that of the commercial FBG sensors in Fig. 2(f) because the ultrafine diameter (12 μm) increased the strain under the common stress and the evanescent field[35,36] introduced the variation in the microfiber's effective refractive index.

The soft μFBG patch also had a great response to low-frequency vibration, benefiting from the ultrathin thickness of the PDMS patch. As shown in Fig. 2(g–i), the waveform was sinusoidal, and the amplitude was identical when detecting vibrations with frequencies of 1 Hz, 2 Hz, and 5 Hz, ensuring waveform accuracy when detecting human physiological mechanical signals, which tend to be low-frequency vibration signals. Also, the μFBG patch can successfully measure vibrations up to 100 Hz (Supplementary information Fig. S3). By designing the structure of the microfiber and the demodulation equipment, higher frequency vibration signals can be acquired[37]. A 10000-circle repetition test was performed with the same stress at a frequency of 1 Hz, as shown in Fig. 2(j), showing the great repeatability and robustness of the soft μFBG patch.

Human physiological signal detection

Owing to the skin-like mechanical compliance and excellent stress/vibration response, the skin-like μFBG patch can maintain stable contact with human skin in different body locations and detect multiple physiological signals. The subjects were instructed to relax their bodies and to remain calm during the measurement. Ballistocardiogram (BCG) signals, as the near-end signals of the cardiovascular system and pulse waves at multiple far-end body sites, were detected to analyze the propagation process of pulse waves and monitor hemodynamic parameters. An FBG interrogator was employed to record the wavelength shift of the soft μFBG patch caused by micro stress on the skin surface due to cardiovascular activity with a sampling frequency of 2500 Hz.

As shown in Fig. 3(a), the soft μFBG patch was attached to the chest skin at the tricuspid site to detect the BCG signal. A small amount of medical alcohol was applied to make the μFBG patch adhere conformally to the skin surface. After the alcohol evaporated, the patch maintained close contact with the skin. The raw BCG signal (Supplementary information Fig. S4(a)) was mixed with the respiration signal caused by the periodic expansion of the chest, which was represented as baseline shift and had a low frequency (< 1 Hz). By employing the short-time Fourier transform (STFT), the time-frequency diagram of the raw BCG signal was obtained (Supplementary information Fig. S4(b)). The frequency components related to heart rate were clearly identified in the time-frequency diagram. Therefore, a 3–15 Hz bandpass filter was employed to eliminate the low-frequency respiration signal and the high-frequency noise. After filtering, the BCG signal relative to periodic cardiovascular activity stood out both in the time domain and in the time-frequency domain (Supplementary information Fig. S4(c) and S4(d)). The heart rate period can be distinguished significantly (see the triangle marks in Fig.

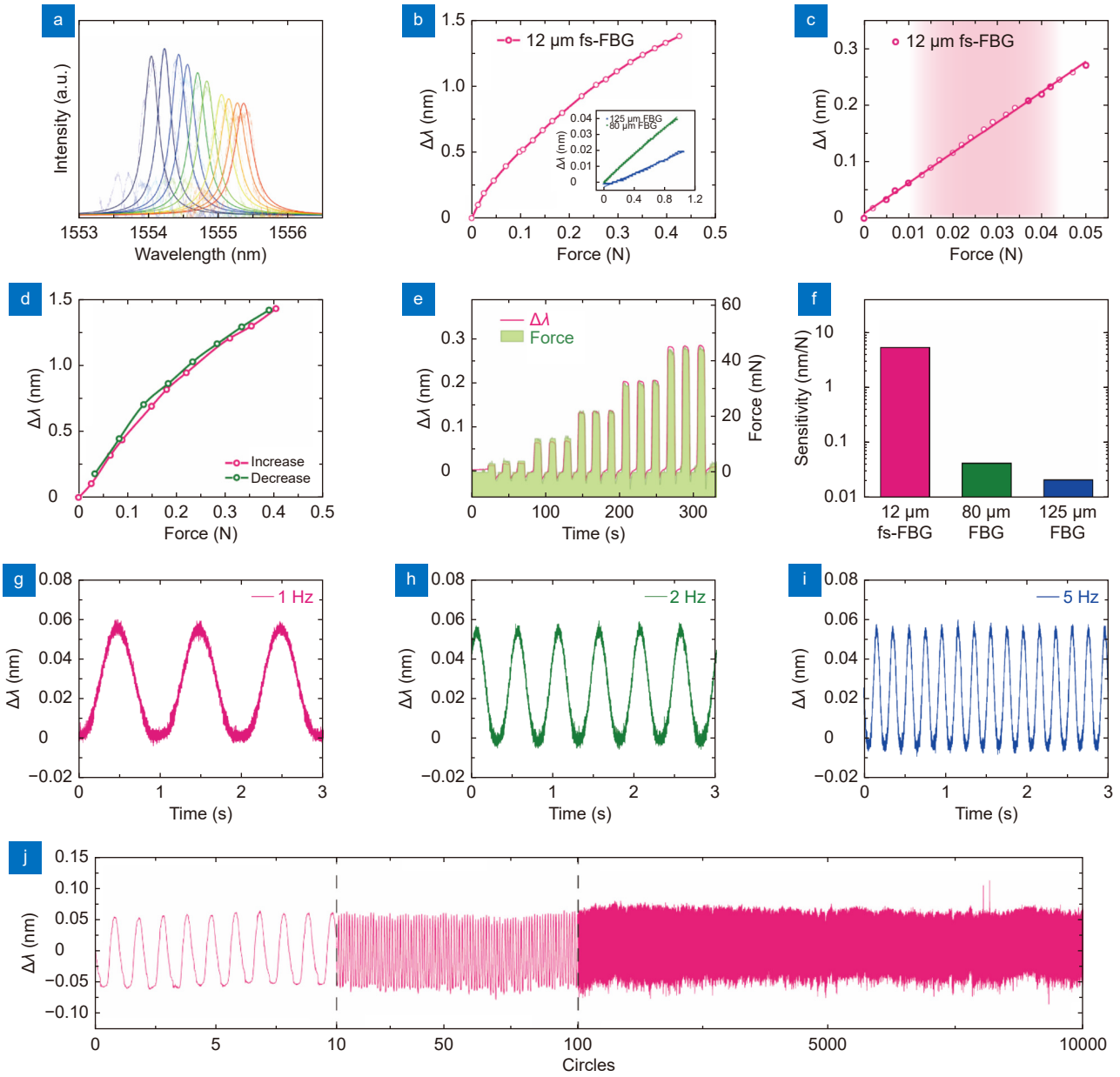

Fig. 2 | Stress and vibration characterization of skin-like μFBG patch. (**a**) Reflective optical spectra of the soft μFBG patch under different stresses. (**b**) Stress response of the soft μFBG patch. (Inset: stress response of the commercial FBG with a diameter of 80 μm and 125 μm separately for comparison.) (**c**) Details of the stress response of the soft μFBG patch when detecting small stresses. The red region indicates the stress range of the life pulse. (**d**) Stress response of the soft μFBG patch when stress increases and decreases to illustrate the hysteresis property. (**e**) Dynamic stress response of the soft μFBG patch compared with a commercial force meter. (**f**) Sensitivity of the soft μFBG patch, which is enhanced by two orders of magnitude compared with commercial FBGs with diameters of 80 μm and 125 μm. (**g–i**) Vibration characterization of the soft μFBG patch under frequencies of 1 Hz, 2 Hz, and 5 Hz. (**j**) 10000-circle repetition tests of the soft μFBG patch to illustrate great repeatability.

3(b)). Figure 3(c) shows the details of BCG signal. Among the feature points, the I wave represents the beginning of cardiac ejection. The purple region identified by the I wave and K wave indicates the systole of the heart rhythm. The spectrum signature of the BCG signal is illustrated in Fig. 3(d).

When detecting the pulse wave, the soft μFBG patch was attached to the skin at the superficial artery sites, as shown in Fig. 3(e). The typical pulse wave at the radial artery is shown in Fig. 3(f). As shown in Supplementary Fig. S4(e) and S4(f), the raw pulse wave contained the baseline shift caused by the movement of the arm and obvious high-frequency noise. Therefore, a 0.5–10 Hz bandpass filter was employed to remove them

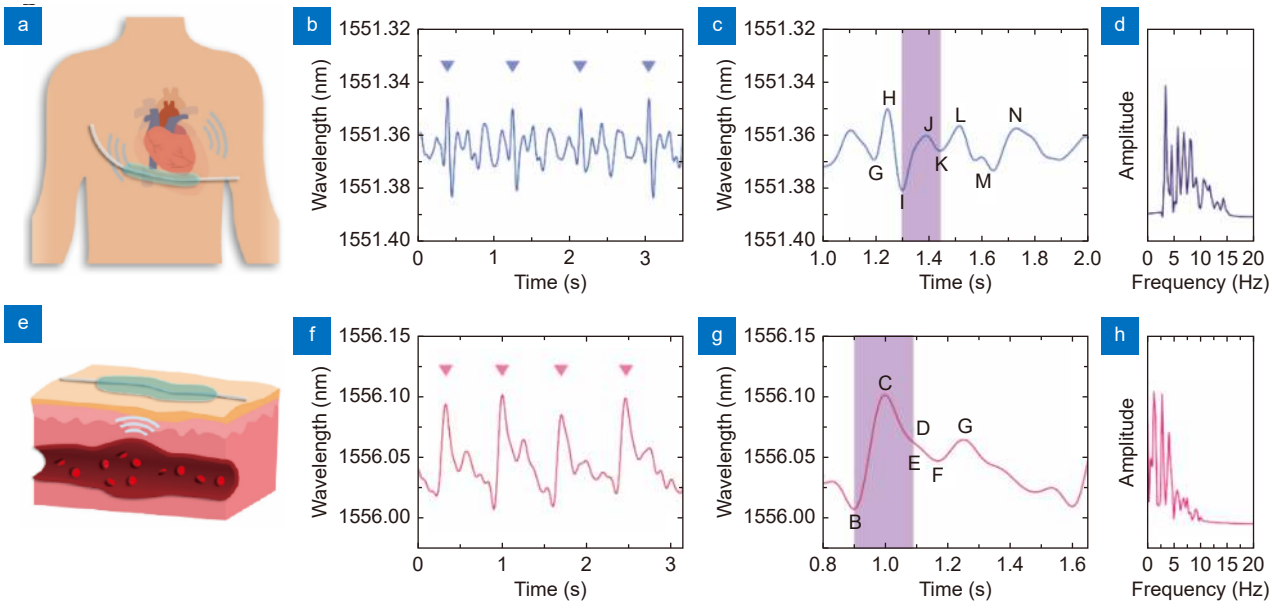

Fig. 3 | Ballistocardiogram (BCG) signal and pulse wave detection using a μFBG patch. (**a**) Schematic diagram of BCG signal detection. A soft μFBG patch is attached to the chest skin at the tricuspid site. (**b**) BCG signal detected by the soft μFBG patch, and the triangle marks indicate the cardiac cycle. (**c**) Details of the BCG signal. The purple region indicates the systole of the rhythm of the heart, which can be identified according to the characteristic I wave and K wave. (**d**) Frequency spectrum of the BCG signal. (**e**) Schematic diagram of pulse wave detection. A soft μFBG patch is attached to the skin at the sites of the superficial arteries. (**f**) Pulse wave detected by the soft μFBG patch, and the triangle marks indicate the cardiac cycle. (**g**) Details of the pulse wave. The purple region indicates the systole of the rhythm of the heart, which can be identified according to the characteristic B wave and E wave. (**h**) Frequency spectrum of pulse wave.

(Supplementary information Fig. S4(g) and S4(h)). Additionally, the details of the pulse wave are shown in Fig. 3(g). The B wave tends to represent the beginning of cardiac ejection, and the purple region identified by the B wave and D wave indicates the systole of the heart rhythm. The spectrum signature of the pulse wave is illustrated in Fig. 3(h). The I wave of the BCG signal and the B wave of the pulse wave both represent the beginning of cardiac ejection. Therefore, we use the two feature points to calculate the PTT and to analyze the propagation process of the pulse wave.

The signal amplitude defined by the maximum wavelength shift is a key factor in determining the signal quality. Benefiting from the high sensitivity of the soft μFBG patch, the signal amplitudes of the BCG signal and radial pulse wave were up to 35 pm and 80 pm, respectively, guaranteeing the accuracy of hemodynamic monitoring. Using the same detection method, the commercial FBG had a signal amplitude of less than 2 pm, which was hard to detect by optical signal acquisitions, resulting in poor waveform accuracy (Supplementary information Fig. S5).

Systemic PTT calculation using the μFBG group

Owing to the multichannel and time-synchronized operation capability, the soft μFBG group was built by connecting two μFBG patches in series. The μFBG group was capable of detecting the BCG signal and pulse wave synchronously. The I wave of the BCG signal and the B wave of the pulse wave were used to calculate the PTT. By detecting the pulse wave at different superficial artery sites, systemic PTT was available to thoroughly evaluate the status of the cardiovascular system. As shown in Fig. 4(a), the PTTs of three different cases (heart to carotid artery (CA), heart to radial artery (RA), and heart to pedal artery (PA)) were detected and calculated on a healthy man with a body height of 172 cm. Figure 4(b–g) shows the waveforms and details of the synchronous BCG signal and pulse wave. The purple regions indicate each PTT.

The morphology of pulse waves at the three superficial artery sites differed from each other. The pulse wave at limbs tended to possess a steeper waveform compared with the one at neck. This phenomenon is caused by the backward propagation of pulse waves at arterioles, which is called the amplification effect[38]. Compared to the central site, such as the neck, the reflected pulse wave at the peripheral site travels a much shorter distance and thus instantly contributes to the waveform, resulting in a higher amplitude. In addition, the pulse wave at limbs tended to have a later dicrotic wave compared with the

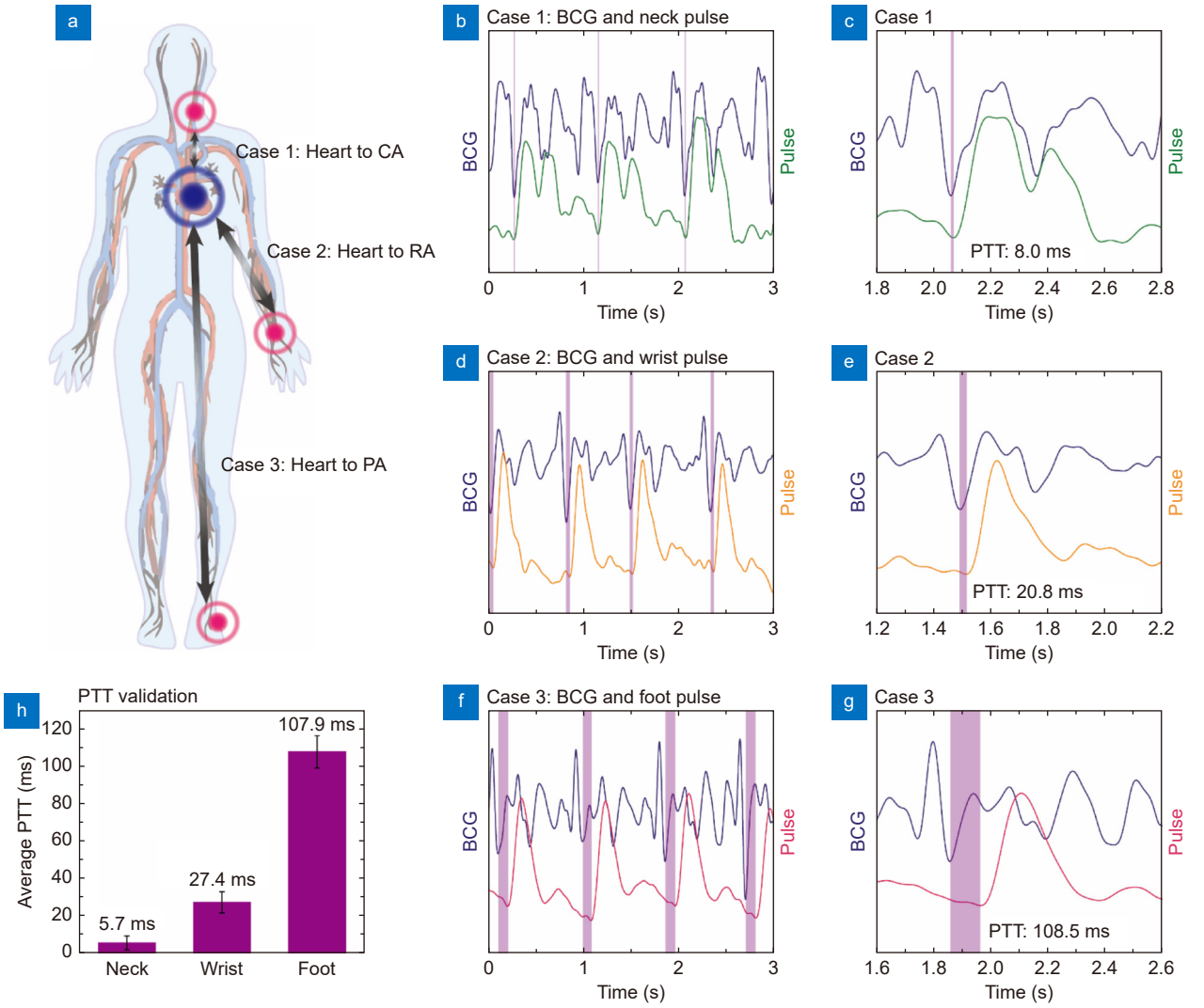

Fig. 4 | Systemic pulse transmit time (PTT) calculation using the soft μFBG group. (**a**) Schematic diagram of the measurement positions for the three cases. Systemic PTTs are calculated via the cooperative analysis of BCG signals and pulse waves at the three different superficial artery sites. (**b**, **c**) Case 1: simultaneous measurement of BCG and pulse wave at the carotid artery (CA). (**d**, **e**) Case 2: simultaneous measurement of BCG and pulse wave at the radial artery (RA). (**f**, **g**) Case 3: simultaneous measurement of BCG and pulse wave at the pedal artery (PA). The graphs (c, e, g) show the details of the BCG signal and pulse wave within one cardiac cycle. The PTTs of the three cases, indicated by the purple region, are identified by the I wave of the BCG and the B wave of the pulse wave. (**h**) Comparison of the average PTT results of the three cases to illustrate the systemic hemodynamic evaluation ability of the soft μFBG group.

wave at the neck. The dicrotic wave is generated from the blood reflux flowing to the artery again due to the closure of the aortic valve. For the pulse wave at peripheral sites, the blood reflux travels a longer distance from the heart, thus contributing to the increasing time interval between the systolic peak and the dicrotic wave.

The PTTs of the three cases differed from each other, as shown in Fig. 4(h). The pulse wave propagating from the heart to the CA needed the shortest PTT of 5.7 ms in the average. In comparison, the average PTTs of the heart to the RA and the heart to the PA were 27.4 ms and 107.9 ms, respectively. The validation of PTT is due to the different artery lengths and pulse wave propagation velocity. The pulse wave at the aorta has a relatively slow PWV (~5 m/s) because of the large elastic modulus[39], and the pulse wave at the arteriole has a quick PWV (15–35 m/s)[40]. Therefore, the PTT from the heart to the CA was very short, and the pulse wave propagating from the heart to the PA required a long time considering an artery length of more than 1 meter. Relying on the multichannel and time-synchronized operation capability, the soft μFBG group realized systemic PTT calculation. Moreover, it is capable of detecting the all-mechanical process of pulse wave propagation and achieving a more

accurate propagation time of pulse waves than pulse arrival time (PAT) by eliminating the pre-ejection period (PEP) delay[41]. Based on the above advantages, the μFBG group demonstrates the potential for accurate clinical diagnosis and early screening of lesions in the cardiovascular system.

Hemodynamic monitoring during exercise

Under the load from exercise, there are many changes in hemodynamics due to increasing metabolism. Research on hemodynamic variation law during exercise can provide an early diagnosis of cardiovascular disease and comprehensively evaluate cardiovascular system function[42,43]. Unlike a commercial cuff-type sphygmomanometer, the soft μFBG group is capable of detecting physiological signals in real time and monitoring hemodynamics continuously. Supplementary information Fig. S6 shows an operational flowchart of hemodynamic monitoring using the soft μFBG group. One patch of the μFBG group was attached to the chest skin, and the other was attached to the left foot. After signal filtering, the near-end BCG signal, far-end pulse wave, and respiration signal were extracted with great temporal synchronization, as shown in Fig. 5(a). The I wave of the BCG signal and the B wave of the pulse wave were used to calculate the HR and PTT. The subject lay on the bed and exercised by pretending to ride a bicycle with the right foot alone. At the same time, a commercial cuff-type sphygmomanometer was employed on the left arm of the subject to provide the gold standard HR and BP. Figure 5(b) and 5(c) demonstrate typical waveforms of the BCG signal and pulse wave when the subject was in static and in exercise, respectively. As shown in Fig. 5(d), the HR was increased at the beginning of exercise and decreased to a normal level after 3–4 minutes at the end of exercise. The BCG signal and pulse wave at several typical time points are shown in Supplementary information Fig. S7. At the same time interval, there are more cardiac cycles in exercise than in static. The HR achieved by the soft μFBG group was consistent with the results of the sphygmomanometer, showing the accuracy of hemodynamic monitoring. During exercise, another interesting phenomenon was that the PWV (proportional to 1/PTT) significantly increased along with the systolic blood pressure, which is shown in Fig. 5(e). This phenomenon is due to the contraction of nonexercise muscle blood vessels caused by sympathetic stimulation in exercise. The contraction leads to increased arterial pressure and accelerated blood flow. The variation in HR and PTT achieved by the soft μFBG group was repeatable under multiple exercise periods, demonstrating the potential for dynamic hemodynamic monitoring.

Dynamic peripheral resistance monitoring

PR reflects the unobstructed level of the cardiovascular system, and PR monitoring is significant for the diagnosis of cardiovascular diseases such as arteriosclerosis, thrombus, and hypertension[44,45]. Relying on the PTT, the dynamic variation in PR was successfully monitored by our soft μFBG group. Figure 6(a) shows a schematic diagram of the PR monitoring experiment. One patch of the μFBG group was attached to the chest skin to detect the BCG signal, and the other was attached to the left wrist to detect the pulse wave. An inflatable cuff was employed at the left upper arm to impose external pressure on the artery to simulate the variation in PR. The external pressure rapidly increased and slowly decreased in the process. The continuous BCG signal and pulse wave are shown in Fig. 6(b), and the green region indicates the compression period. The BCG signal was stable, but the pulse wave was disturbed and even interrupted because high external pressure blocked the blood flow. It is a notable feature that PTT increased with the external pressure when the pulse waveform was recognizable. When the external pressure increased, the transmural blood pressure defined by the differential value between the internal pressure (also known as BP) and external pressure of the artery decreased, resulting in slow PWV (for a detailed analytical model of the artery, see Supplementary information *Materials and methods* and Fig. S9). The response of PTT to the external pressure was reproducible, demonstrating the soft μFBG group's potential for PR monitoring. Benefiting from the multichannel operation capability, the soft μFBG group can monitor the regional PR of the artery and have a potential application in rapid thrombus positioning.

Conclusions

We have demonstrated a soft μFBG group that offers continuous and noninvasive monitoring of spatiotemporal hemodynamics. Combining flexible material integration with precise micro/nanostructure design, the soft μFBG patch achieves both a great sensing response on stress/vibration and intimate coupling with human skin with suitable mechanical compliance. Thanks to its ultrafine diameter and ultrathin thickness, this sensor's sensitivity has been increased by two orders of magnitude compared to commercial FBGs. Exploiting the

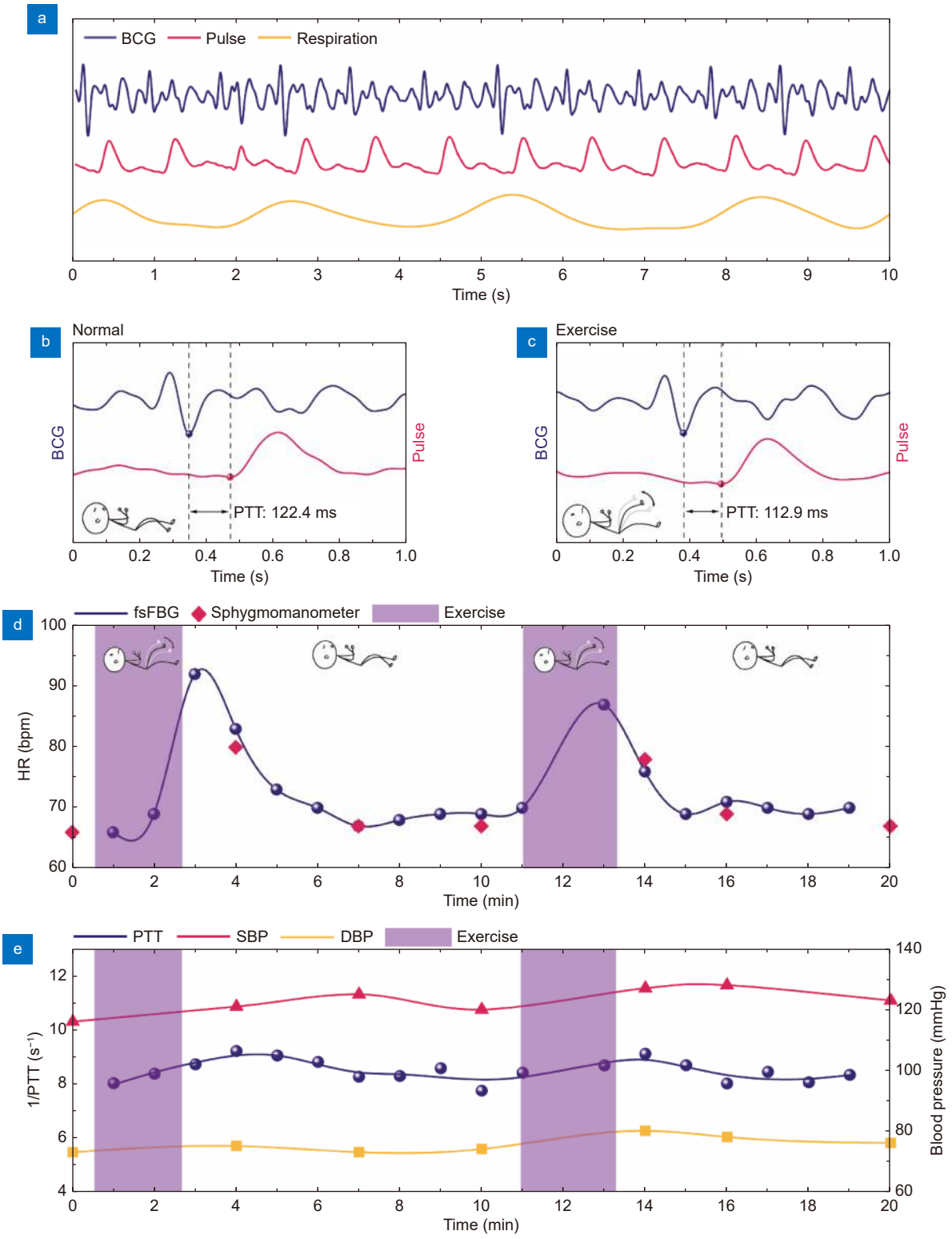

Fig. 5 | Hemodynamic monitoring during exercise using soft μFBG group. (**a**) Representative BCG signal (blue), pulse wave at the PA site (red), and respiration signal (yellow) monitored simultaneously. (**b**, **c**) Details of the synchronized BCG signal and pulse wave during the normal state and exercise state, respectively. PTT is indicated by the dashed lines. (**d**) Comparison of heart rate (HR) calculated from the vital signal acquired by the μFBG group (blue) and a commercial sphygmomanometer (red). (**e**) Comparison of PTT (blue), which is calculated from the BCG signal and pulse wave acquired by the μFBG group, and the systolic and diastolic blood pressure (SBP and DBP) acquired from a commercial sphygmomanometer. The exercise periods are indicated by the purple region.

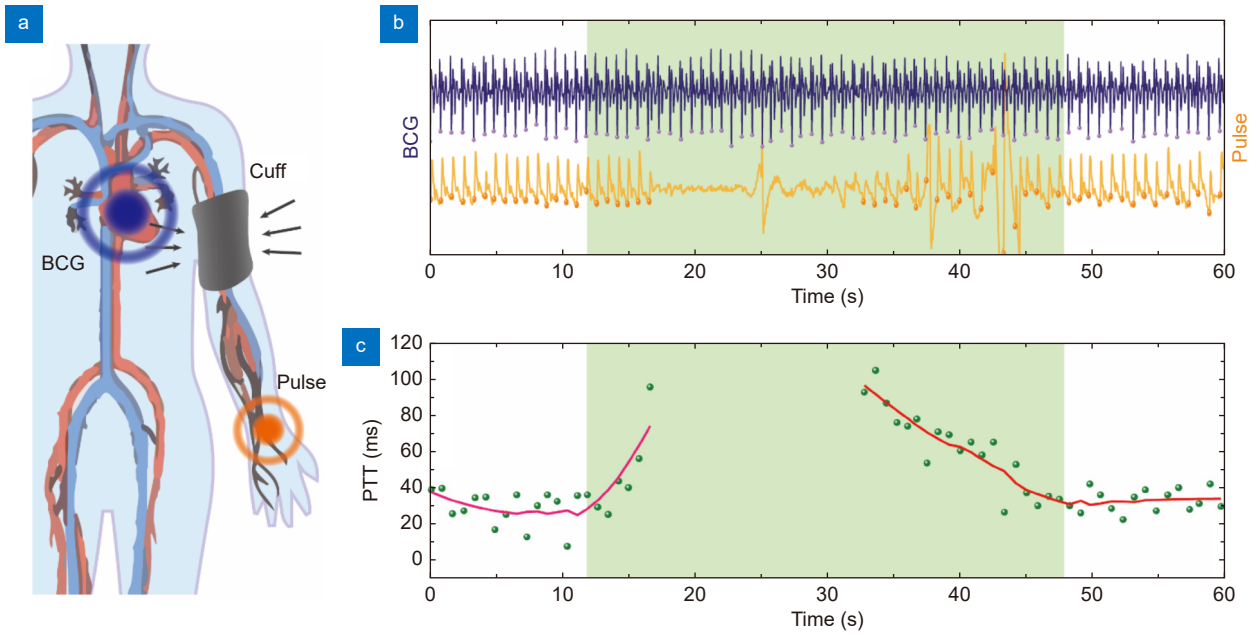

Fig. 6 | Peripheral resistance monitoring using soft μFBG group. (**a**) Schematic diagram of peripheral resistance monitoring. An inflatable cuff is used to impose the external pressure on the artery. The BCG signal and pulse wave at the RA site are continuously detected to calculate the PTT. (**b**) BCG signal (blue) and pulse wave (yellow) detected simultaneously by μFBG group. (**c**) PTT of every cardiac cycle (green dot) calculated from the vital signal. The trend of PTT indicated by the red line is calculated by moving averaging. The compression periods are indicated by the green region.

advanced femtosecond laser fabrication technique and quasi-distributed optical fiber sensing technique, high-quality all-mechanical physiological signals such as the near-end BCG signal and far-end pulse wave are detected to reflect the actual mechanical process of blood circulation. Relying on the multichannel and time-synchronized operation capability, the soft μFBG group can be used to monitor systemic hemodynamic parameters and reflect regional artery statuses. The device satisfies clinical requirements for real-time and continuous hemodynamic monitoring and reconfigurable regional health evaluation of the cardiovascular system. In addition, electromagnetic immunity makes the μFBG group compatible with essential medical imaging, especially magnetic resonance imaging. Applications in systemic PTT calculation, dynamic hemodynamic monitoring during exercise, and regional PR monitoring demonstrate the great potential in the diagnosis of cardiovascular diseases such as arrhythmia, angiosclerosis, hypertension, and thrombosis and can facilitate precise clinical diagnosis, the fast screening of lesions, and daily health management.

References

1. Dagenais GR, Leong DP, Rangarajan S, Lanas F, Lopez-Jaramillo P et al. Variations in common diseases, hospital admissions, and deaths in middle-aged adults in 21 countries from five continents (PURE): a prospective cohort study. *Lancet* **395**, 785–794 (2020).
2. Kaur RI. Electrocardiogram signal analysis - an overview. *Int J Comput Appl* **84**, 22–25 (2013).
3. Debbal SM, Bereksi-Reguig F. Computerized heart sounds analysis. *Comput Biol Med* **38**, 263–280 (2008).
4. Elgendi M. On the analysis of fingertip photoplethysmogram signals. *Curr Cardiol Rep* **8**, 14–25 (2012).
5. Allen J. Photoplethysmography and its application in clinical physiological measurement. *Physiol Meas* **28**, R1–R39 (2007).
6. Buxi D, Redouté JM, Yuce MR. A survey on signals and systems in ambulatory blood pressure monitoring using pulse transit time. *Physiol Meas* **36**, R1–R26 (2015).
7. Chen Y, Wen CY, Tao GC, Bi M. Continuous and noninvasive measurement of systolic and diastolic blood pressure by one mathematical model with the same model parameters and two separate pulse wave velocities. *Ann Biomed Eng* **40**, 871–882 (2012).
8. Chen Y, Wen CY, Tao GC, Bi M, Li GQ. Continuous and noninvasive blood pressure measurement: a novel modeling methodology of the relationship between blood pressure and pulse wave velocity. *Ann Biomed Eng* **37**, 2222–2233 (2009).
9. Ding XR, Yan BP, Zhang YT, Liu J, Zhao N et al. Pulse transit time based continuous cuffless blood pressure estimation: a new extension and a comprehensive evaluation. *Sci Rep* **7**, 11554 (2017).
10. Mukkamala R, Hahn JO, Inan OT, Mestha LK, Kim CS et al. Toward ubiquitous blood pressure monitoring via pulse transit time: theory and practice. *IEEE Trans Biomed Eng* **62**, 1879–1901 (2015).
11. Sharma M, Barbosa K, Ho V, Griggs D, Ghirmai T et al. Cuff-less and continuous blood pressure monitoring: a methodological review. *Technologies* **5**, 21 (2017).
12. Koo JH, Yun HW, Lee WC, Sunwoo SH, Shim HJ et al. Recent advances in soft electronic materials for intrinsically stretchable optoelectronic systems. *Opto-Electron Adv* **5**, 210131 (2022).

13. Bennett A, Beiderman Y, Agdarov S, Beiderman Y, Hendel R et al. Monitoring of vital bio-signs by analysis of speckle patterns in a fabric-integrated multimode optical fiber sensor. *Opt Express* **28**, 20830–20844 (2020).
14. Chung HU, Kim BH, Lee JY, Lee J, Xie ZQ et al. Binodal, wireless epidermal electronic systems with in-sensor analytics for neonatal intensive care. *Science* **363**, eaau0780 (2019).
15. Chung HU, Rwei AY, Hourlier-Fargette A, Xu S, Lee K et al. Skin-interfaced biosensors for advanced wireless physiological monitoring in neonatal and pediatric intensive-care units. *Nat Med* **26**, 418–429 (2020).
16. Jin Y, Chen GN, Lao KT, Li SH, Lu Y et al. Identifying human body states by using a flexible integrated sensor. *npj Flex Electron* **4**, 28 (2020).
17. Li HC, Ma YJ, Liang ZW, Wang ZH, Cao Y et al. Wearable skin-like optoelectronic systems with suppression of motion artifacts for cuff-less continuous blood pressure monitor. *NatI Sci Rev* **7**, 849–862 (2020).
18. Zhong F, Hu W, Zhu PN, Wang H, Ma C et al. Piezoresistive design for electronic skin: from fundamental to emerging applications. *Opto-Electron Adv* **5**, 210029 (2022).
19. Li JH, Chen JH, Xu F. Sensitive and wearable optical microfiber sensor for human health monitoring. *Adv Mater Technol* **3**, 1800296 (2018).
20. Wang CH, Li XS, Hu HJ, Zhang L, Huang ZL et al. Monitoring of the central blood pressure waveform via a conformal ultrasonic device. *Nat Biomed Eng* **2**, 687–695 (2018).
21. Zhang L, Pan J, Zhang Z, Wu H, Yao N et al. Ultrasensitive skin-like wearable optical sensors based on glass micro/nanofibers. *Opto-Electron Adv* **3**, 190022 (2020).
22. Zhu HT, Zhan LW, Dai Q, Xu B, Chen Y et al. Self‐assembled wavy optical microfiber for stretchable wearable sensor. *Adv Opt Mater* **9**, 2002206 (2021).
23. Hill KO, Meltz G. Fiber Bragg grating technology fundamentals and overview. *J Lightwave Technol* **15**, 1263–1276 (1997).
24. Dziuda Ł, Skibniewski FW. A new approach to ballistocardiographic measurements using fibre Bragg grating-based sensors. *Biocybern Biomed Eng* **34**, 101–116 (2014).
25. Haseda Y, Bonefacino J, Tam HY, Chino S, Koyama S et al. Measurement of pulse wave signals and blood pressure by a plastic optical fiber FBG sensor. *Sensors* **19**, 5088 (2019).
26. Xu L, Liu N, Ge J, Wang XQ, Fok MP. Stretchable fiber-Bragg-grating-based sensor. *Opt Lett* **43**, 2503–2506 (2018).
27. Al-Fakih EA, Abu Osman NA, Mahamd Adikan FR, Eshraghi A, Jahanshahi P. Development and validation of fiber Bragg grating sensing pad for interface pressure measurements within prosthetic sockets. *IEEE Sensors J* **16**, 965–974 (2016).
28. Li TL, Su YF, Chen FY, Liao XQ, Wu Q et al. A skin‐like and highly stretchable optical fiber sensor with the hybrid coding of wavelength–light intensity. *Adv Intell Syst* **4**, 2100193 (2022).
29. Pan J, Zhang Z, Jiang CP, Zhang L, Tong LM. A multifunctional skin-like wearable optical sensor based on an optical micro-/nanofibre. *Nanoscale* **12**, 17538–17544 (2020).
30. Ma SQ, Wang XY, Li P, Yao N, Xiao JL et al. Optical Micro/Nano fibers enabled smart textiles for human–machine interface. *Adv Fiber Mater* **4**, 1108–1117 (2022).
31. Brambilla G, Finazzi V, Richardson DJ. Ultra-low-loss optical fiber nanotapers. *Opt Express* **12**, 2258–2263 (2004).
32. Lou JY, Wang YP, Tong LM. Microfiber optical sensors: a review. *Sensors* **14**, 5823–5844 (2014).
33. Thomas J, Voigtländer C, Becker RG, Richter D, Tünnermann A et al. Femtosecond pulse written fiber gratings: a new avenue to integrated fiber technology. *Laser Photonics Rev* **6**, 709–723 (2012).
34. Luo JX, Liu S, Chen PJ, Lu SZ, Zhang Q et al. Fiber optic hydrogen sensor based on a Fabry-Perot interferometer with a fiber Bragg grating and a nanofilm. *Lab Chip* **21**, 1752–1758 (2021).
35. Brambilla G, Xu F, Horak P, Jung Y, Koizumi F et al. Optical fiber nanowires and microwires: fabrication and applications. *Adv Opt Photonics* **1**, 107–161 (2009).
36. Tong LM, Zi F, Guo X, Lou JY. Optical microfibers and nanofibers: a tutorial. *Opt Commun* **285**, 4641–4647 (2012).
37. Yang LY, Li YP, Fang F, Li LY, Yan ZJ et al. Highly sensitive and miniature microfiber-based ultrasound sensor for photoacoustic tomography. *Opto-Electron Adv* **5**, 200076 (2022).
38. Mukkamala R, Xu D. Continuous and less invasive central hemodynamic monitoring by blood pressure waveform analysis. *Am J Physiol Heart Circ Physiol* **299**, H584–H599 (2010).
39. Laurent S, Boutouyrie P, Asmar R, Gautier I, Laloux B et al. Aortic stiffness is an independent predictor of all-cause and cardiovascular mortality in hypertensive patients. *Hypertension* **37**, 1236–1241 (2001).
40. Kim J, Song TJ, Song D, Lee KJ, Kim EH et al. Brachial-ankle pulse wave velocity is a strong predictor for mortality in patients with acute stroke. *Hypertension* **64**, 240–246 (2014).
41. Zhang GQ, Gao MW, Xu D, Olivier NB, Mukkamala R. Pulse arrival time is not an adequate surrogate for pulse transit time as a marker of blood pressure. *J Appl Physiol* **111**, 1681–1686 (2011).
42. Rueckert PA, Slane PR, Lillis DL, Hanson P. Hemodynamic patterns and duration of post-dynamic exercise hypotension in hypertensive humans. *Med Sci Sports Exerc* **28**, 24–32 (1996).
43. Ohlsson Å, Steinhaus D, Kjellström B, Ryden L, Bennett T. Central hemodynamic responses during serial exercise tests in heart failure patients using implantable hemodynamic monitors. *Eur J Heart Fail* **5**, 253–259 (2003).
44. Intengan HD, Schiffrin EL. Structure and mechanical properties of resistance arteries in hypertension: role of adhesion molecules and extracellular matrix determinants. *Hypertension* **36**, 312–318 (2000).
45. Taylor AJ, Bobik A, Berndt MC, Ramsay D, Jennings G. Experimental rupture of atherosclerotic lesions increases distal vascular resistance: a limiting factor to the success of infarct angioplasty. *Arterioscler Thromb Vasc Biol* **22**, 153–160 (2002).

Acknowledgements

The project was supported by the National Key R&D Program of China (2021YFA1401103), and the National Natural Science Foundation of China (61925502 and 51772145).

Author contributions

All authors provided active and valuable feedback on the manuscript.

F. Xu, H. T. Zhu, J. X. Luo, and Q. Dai initiated the concept and designed the studies; F. Xu. supervised the work; H. T. Zhu, J. X. Luo, S. G. Zhu, and H. Yang led the experiments and collected the overall data; Q. Dai and B. Xu contributed to the design of the human studies; K. H. Zhou contributed to sensor preparation; L. W. Zhan contributed to the design of the peripheral resistance studies. Y. Chen and Y. Q. Lu advised on the experiments. F. Xu, H. T. Zhu, J. X. Luo, and Q. Dai co-wrote the paper.

Competing interests

The authors declare no competing financial interests.

Supplementary information

Supplementary information for this paper is available at https://doi.org/10.29026/oea.2023.230018